KeAi
CHINESE ROOTS
GLOBAL IMPACT

Available online at www.sciencedirect.com

ScienceDirect

Green Energy & Environment 9 (2024) 1151−1158

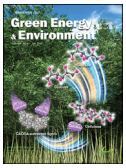

www.keaipublishing.com/gee

Research paper

Surface-neutralization engineered NiCo-LDH/phosphate hetero-sheets toward robust oxygen evolution reaction

Shunfa Zhou [a], Yuxuan Liu [a], Jing Li [a], Zhao Liu [a], Jiawei Shi [a], Liyuan Fan [b], Weiwei Cai [a,*]

[a] *Sustainable Energy Laboratory, Faculty of Materials Science and Chemistry, China University of Geosciences, Wuhan, 430074, China*
[b] *College of Science and Engineering, James Cook University, 1 James Cook Drive, Townsville, QLD, 4811, Australia*

Received 30 October 2022; revised 24 November 2022; accepted 9 December 2022
Available online 14 December 2022

Abstract

Developing highly active oxygen evolution reaction (OER) electrocatalysts with robust durability is essential in producing high-purity hydrogen through water electrolysis. Layered double hydroxide (LDH) based catalysts have demonstrated efficient catalytic performance toward the relatively sluggish OER. By considering the promotion effect of phosphate (Pi) on proton transfer, herein, a facile phosphate acid (PA) surface-neutralization strategy is developed to in-situ construct NiCo-LDH/NiCoPi hetero-sheets toward OER catalysis. OER activity of NiCo-LDH is significantly boosted due to the proton promotion effect and the electronic modulation effect of NiCoPi. As a result, the facilely prepared NiCo-LDH/NiCoPi catalyst displays superior OER catalytic activity with a low overpotential of 300 mV to deliver 100 mA cm^{-2} OER and a Tafel slope of 73 mV dec^{-1}. Furthermore, no visible activity decay is detected after a 200-h continuous OER operation. The present work, therefore, provides a promising strategy to exploit robust OER electrocatalysts for commercial water electrolysers.

Keywords: Oxygen evolution reaction; Phosphate; Layered double hydroxide; Hetero-sheets; Stability

1. Introduction

Hydrogen is one of the most promising clean energy sources by its high gravimetric density and environmental-friendly feature [1–4]. Electrochemical water splitting, which involves two half-reactions: hydrogen evolution reaction (HER) and oxygen evolution reaction (OER), is an effective and sustainable pathway for hydrogen production [5–8]. OER is a multiple electron transfer process, and the sluggish dynamics make it the choke point in high-efficiency water electrolysis [5,9,10]. Nobel-metal-based oxides (RuO_2/IrO_2) are regarded as OER electrocatalysts with high electrocatalytic activity [11]. However, their inadequate durability and scarce earth reserves seriously impede their industrial application [12–14]. Therefore, exploiting earth-abundant, efficient and robust OER electrocatalysts is attracting more and more attention [15,16].

Various transition metal (TM) materials have been researched as OER electrocatalysts [17–20]. TM layered double hydroxides (LDHs) are promising OER electrocatalysts because of their adjustable composition, low-toxic and unique two-dimensional layered structure [21–23]. Numerous methods have been exploited to enhance the OER performance of LDHs, such as morphology engineering, defects engineering and heterostructure engineering [24,25]. Many attempts are performed to improve the OER electrocatalytic activity of LDHs through heterostructure engineering modulation. The heterostructure engineering method is efficient in modulating the catalytic performance by precisely tuning the electronic structure of metal sites and regulating charge transfer in the OER process [26]. Liu et al. [27] reported a Ni_3S_2@NiV-LDH hetero-sheet array supported on

* Corresponding author.
E-mail addresses: willcai1985@gmail.com, caiww@cug.edu.cn (W. Cai).

https://doi.org/10.1016/j.gee.2022.12.003

nickel foam, benefiting from the large interfaces and enhanced electronic interactions, an overpotential of 320 mV to deliver 100 mA cm^{-2} OER was achieved. Song et al. [28] constructed $CoSe_2$@CoNi LDH hybrid nanostructured arrays on a carbon cloth; the promoted reaction kinetics induced by the strong interaction of interface greatly enhance the OER performance. This catalyst only needs a low overpotential of 240 mV to deliver 10 mA cm^{-2} OER. However, developing a facile and universal strategy for heterostructure construction is still required and challenging for TM-LDH-based OER catalysts.

TM phosphates (Pi) have also recently received significant attention as OER catalysts [29–32]. The phosphate groups in Pi can act as the proton acceptor, promote the proton-transfer kinetics and tune the electronic characteristic of active sites due to their substantial nucleophilic properties, which are beneficial for OER catalysis [33–35]. Besides, the hydrophilic nature of Pi can enable fast mass transfer between the electrolyte and catalyst [36]. Therefore, combining Pi with LDH is reasonable to enhance the electrocatalytic OER activity of LDH. A facile and universal approach to constructing NiCo-LDH/NiCoPi hetero-sheets is reported for the first time via a simple phosphate acid (PA) surface neutralization strategy. The surface of NiCo-LDH is partially converted to amorphous NiCoPi via the neutralization reaction of PA with NiCo-LDH, and LDH/NiCoPi hetero-sheets were, therefore, facilely engineered (Fig. 1a). Meanwhile, the etching effect of PA simultaneously creates additional vacancies and exposes more active sites for OER. Consequently, the NiCo-LDH/NiCoPi catalyst with abundant LDH/NiCoPi heterointerfaces only needs 300 mV overpotential to deliver 100 mA cm^{-2} OER in 1 mol L^{-1} KOH electrolyte, which is 73 mV lower than that of the NiCo-LDH catalyst. Further, OER can continuously operate for more than 200 h on the NiCo-LDH/NiCoPi catalyst without any visible activity decay. This surface-neutralization-based LDH/Pi hetero-sheets engineering strategy can apply to other TM-LDHs, such as CoMn-LDH and NiCoMn-LDH, for OER performance enhancement.

2. Experimental

2.1. Synthesis of NiCo-LDH, CoMn-LDH and NiCoMn-LDH

Prior to the LDH synthesis, NF pieces were washed with acetone, 1 mol L^{-1} HCl and deionized water to remove the organic contaminant and oxide shell on the NF surface. NiCo-LDH was grown on the NF surface using a modified hydrothermal reaction. 2.25 mmol $Ni(NO_3)_2 \cdot 6H_2O$ and 0.75 mmol $Co(NO_3)_2 \cdot 6H_2O$ are dissolved in a mixed solution of methanol (60 mL) and deionized water (12 mL) first. Next, 1 g cetyltrimethylammonium bromide (CTAB) was added to the above solution under stirring for 0.5 h to form a transparent solution. Afterwards, a piece of NF (3 cm × 7 cm) was immersed in a stainless-steel autoclave containing the above solution. The autoclave was then heated at 180 °C for 24 h for a hydrothermal reaction. The NF-supported NiCo-LDH sheets were obtained after being washed with deionized water. The synthesis process of CoMn-LDH on NF is analogous to NiCo-

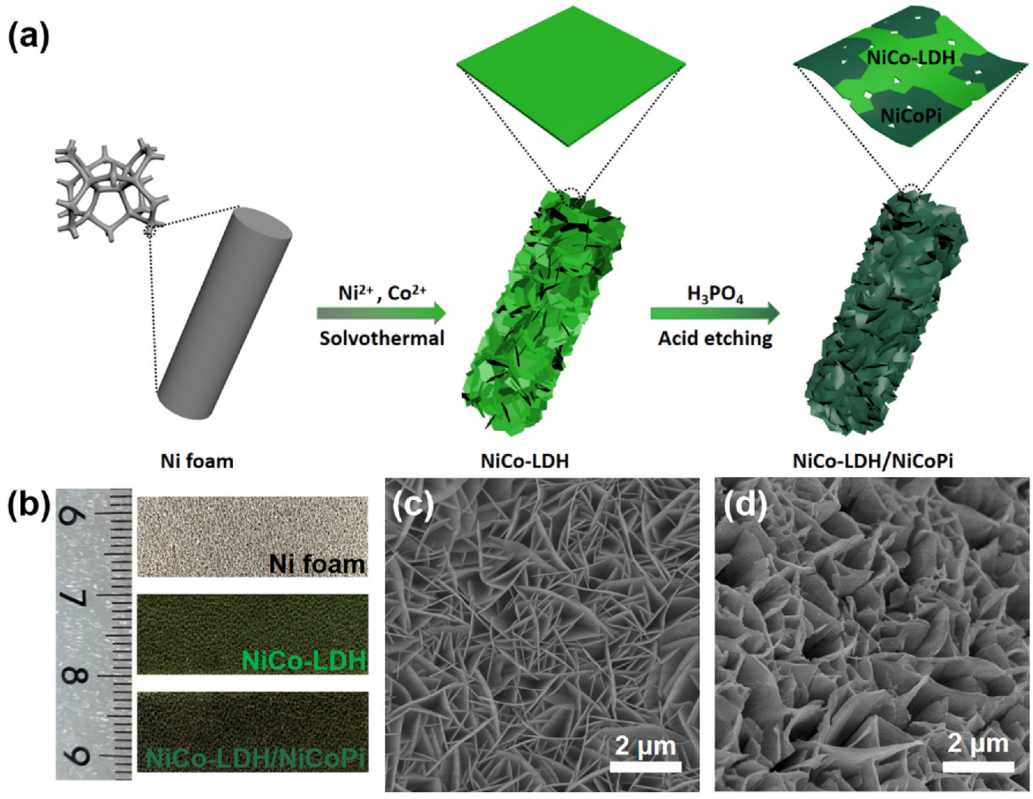

Fig. 1. (a) Diagrammatic illustration for the fabrication of NiCo-LDH/NiCoPi. (b) Optical images of bare NF, NiCo-LDH and NiCo-LDH/NiCoPi; SEM images of (c) NiCo-LDH and (d) NiCo-LDH/NiCoPi.

LDH by substituting $Ni(NO_3)_2 \cdot 6H_2O$ with $Mn(NO_3)_2 \cdot 4H_2O$ instead. The fabrication process of NiCoMn-LDH on NF is also similar to NiCo-LDH, by substituting 2.25 mmol $Ni(NO_3)_2 \cdot 6H_2O$, 0.75 mmol $Co(NO_3)_2 \cdot 6H_2O$ to 1.00 mmol $Ni(NO_3)_2 \cdot 6H_2O$, 1.00 mmol $Co(NO_3)_2 \cdot 6H_2O$ and 1.00 mmol $Mn(NO_3)_2 \cdot 4H_2O$.

2.2. Synthesis of NiCo-LDH/NiCoPi, CoMn-LDH/CoMnPi and NiCoMn/NiCoMnPi

Typically, 0.1 mL 85% PA aqueous solution was added to 10 mL ethanol. After stirring at room temperature for 10 min, a piece of NF (1 cm × 3 cm) supported NiCo-LDH was immersed into a stainless steel autoclave containing the above solution. The autoclave was heated at 100 °C for 6 h for PA surface neutralization. After being dried at 50 °C for 6 h, NiCo-LDH/NiCoPi was successfully obtained. CoMn-LDH/CoMnPi and NiCoMn-LDH/NiCoMnPi were prepared following a similar process for NiCo-LDH/NiCoPi.

Details on physical characterizations and electrochemical measurements are provided in Supporting Information.

3. Results and discussions

3.1. Physical characterizations

As shown in Fig. 1b, the colour changed from the light green of NiCo-LDH to the dark green of NiCo-LDH/NiCoPi after surface-neutralization. The concentration of PA used for surface-neutralization can remarkably affect the OER activity of the NiCo-LDH/NiCoPi catalyst. A PA concentration of ca. 1% (0.1 mL PA in 10 mL ethanol solution) led to the best OER catalytic activity, hence was selected as the delegate sample (Fig. S1). Unlike the smooth surface of bare NF (Fig. S2), SEM images of NiCo-LDH (Fig. 1c and Fig. S3a) demonstrate that NiCo-LDH nanosheets are vertically grown on the NF skeleton. After PA surface-neutralization, the NiCo-LDH/NiCoPi hetero-sheets become thicker than NiCo-LDH sheets, which is ascribed to the formation of NiCoPi. Besides, the hetero-sheets show curved morphology with a rough surface (Fig. 1d and Fig. S3b), which not only increase the surface area and expose more active sites but also promote the permeation of electrolyte for fast mass transport [37].

As shown in the TEM image of NiCo-LDH (Fig. 2a), the flat characteristic of NiCo-LDH can be observed clearly. The clear diffraction rings and the distinct diffraction dots suggest the polycrystalline character of NiCo-LDH (Fig. 2b). The high-resolution TEM (HR-TEM) image was also recorded, in which the lattice fringes were measured to be 0.23 and 0.19 nm, corresponding to (015) and (018) planes of NiCo-LDH (Fig. 2c), respectively. After the surface-neutralization, the TEM image (Fig. 2d) of the NiCo-LDH/NiCoPi hetero-sheet shows a ruffled structure, and the broad rings with indistinct diffraction dots in the SAED pattern indicate the crystallinity decrease (Fig. 2e). The amorphous region in the HR-TEM image (Fig. 2f) corresponds to the NiCoPi phase. The interface between NiCo-LDH and NiCoPi could also be observed clearly (dotted line in Fig. 2f), suggesting the successful engineering of the NiCo-LDH/NiCoPi hetero-interfaces. The lattice fringes of NiCo-LDH in NiCo-LDH/NiCoPi are rougher compared with that of pristine NiCo-LDH, indicating that extra defects were generated during the surface-neutralization due to the etching effect of PA.

The lower intensity and broader full width at half maximum (FWHM) of diffraction peaks in the X-ray diffraction (XRD) pattern of NiCo-LDH/NiCoPi compared with NiCo-LDH also suggest the decrease in crystallinity of NiCo-LDH and the formation of amorphous NiCoPi after PA surface-neutralization (Fig. S4). Additionally, the high angle annular dark field scanning transmission electron microscope (HAADF-STEM) image and the corresponding energy dispersive X-Ray spectroscopy (EDX) elemental distribution of NiCo-LDH/NiCoPi confirm the homogeneous distribution of Ni, Co, O and P (Fig. 2g–k). To further confirm the construction of the NiCo-LDH/NiCoPi heterointerface, FT-IR measurements were also performed (Fig. S5). After surface-neutralization, a new peak at 1350 cm^{-1} appeared, attributed to the P═O bond, which can be detected as desired. Additionally, the Raman spectrum of NiCo-LDH/NiCoPi (Fig. S6) displays broadband at ca. 1000 cm^{-1}, which is attributed to P–O vibration in NiCoPi [38].

To characterize the chemical environment and bonding structure of the catalysts, XPS analysis was performed. Survey XPS spectrum of NiCo-LDH/NiCoPi confirms the presence of Ni, Co, O and P (Fig. 3a). The composition of the NiCo-LDH/NiCoPi and NiCo-LDH (Table S1) confirms that the atomic ratios of Ni:Co in both samples are ca. 3:1. The high-resolution Ni 2p spectrum of NiCo-LDH (Fig. 3b) shows two subpeaks at 855.3 and 873.0 eV, assigning to the Ni $2p_{3/2}$ and Ni $2p_{1/2}$ orbitals. Compared with NiCo-LDH, peak positions of Ni $2p_{3/2}$ and Ni $2p_{1/2}$ for NiCo-LDH/NiCoPi shift positively to 856.0 eV and 873.7 eV attributing to the inductive effect as well as strong interactions of LDH and Pi on the NiCo-LDH/NiCoPi heterointerfaces [39]. For the high-resolution Co 2p spectra (Fig. 3c), the peak positions of Co $2p_{3/2}$ (781.2 eV) and Co $2p_{1/2}$ (797.4 eV) for NiCo-LDH/NiCoPi also shift positively compared with those of NiCo-LDH (780.9 and 797.1 eV, respectively). The positively shifted peaks of Co and Ni are attributed to the inductive effect and strong interactions of the phosphate groups with metal sites in NiCo-LDH/NiCoPi. This also has a significant influence in tuning the electronic structure of the metal sites in NiCo-LDH/NiCoPi and thus promotes the oxidation process of metal centres during OER [40,41]. The high-resolution O 1s spectrum for NiCo-LDH can be deconvoluted to three peaks (Fig. 3d), corresponding to the Metal-O (530.6 eV), the hydroxide bond (OH^-) (531.9 eV) and the adsorbed H_2O (533.9 eV). For NiCo-LDH/NiCoPi, the binding energy of the Metal-O shifts positively owing to the formation of the Metal-O-P bond, and a peak at 533.1 eV was newly observed, attributing to the existence of phosphate groups. Further, the asymmetric property of the OH^- subpeak suggests the presence of oxygen vacancies in the catalyst. It has been reported that the ratio of peak area (OH^-/Metal-O) can roughly evaluate the number of

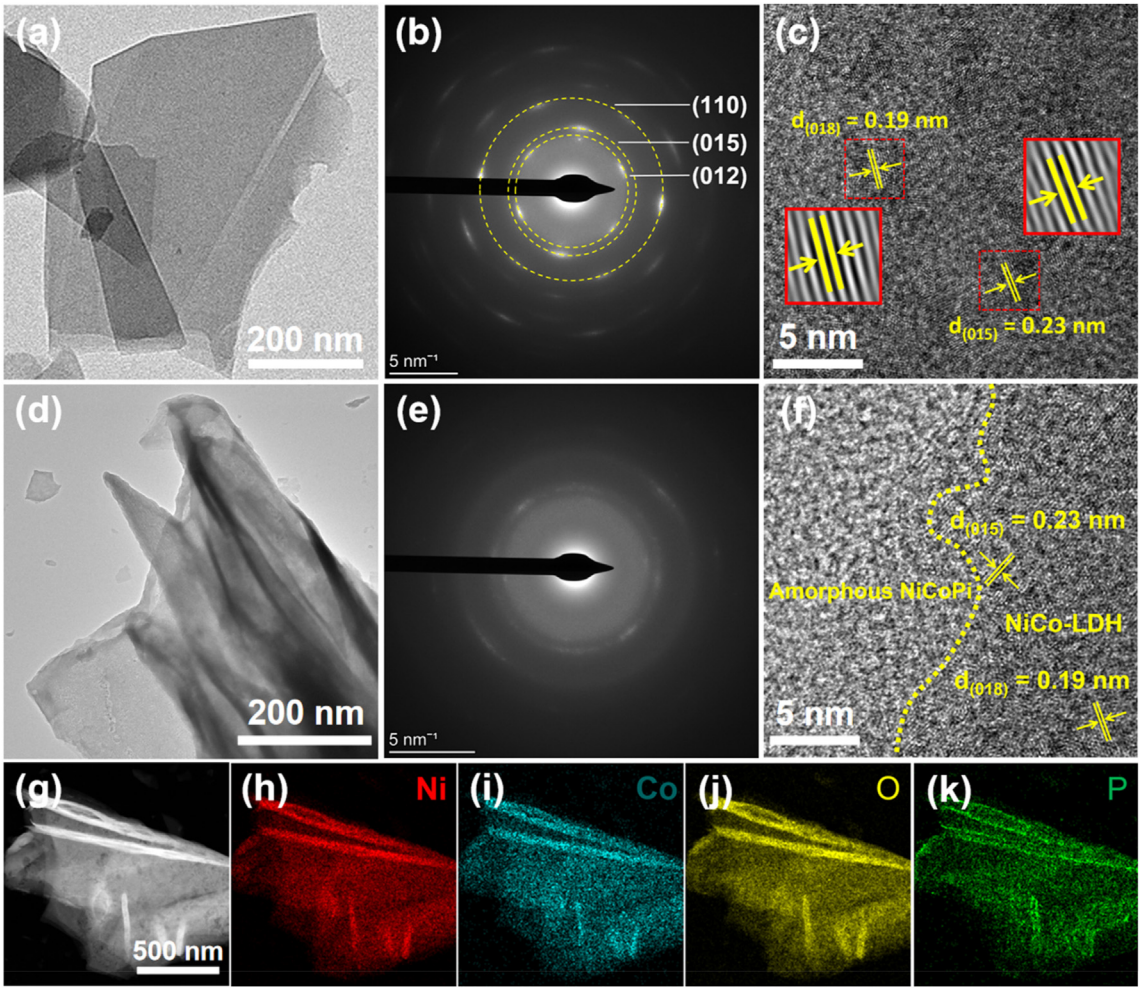

Fig. 2. (a) TEM, (b) SAED and (c) HRTEM images of NiCo-LDH. (d) TEM, (e) SAED and (f) HRTEM images of NiCo-LDH/NiCoPi; (g–k) HAADF-STEM image and the corresponding EDX elemental distribution of NiCo-LDH/NiCoPi.

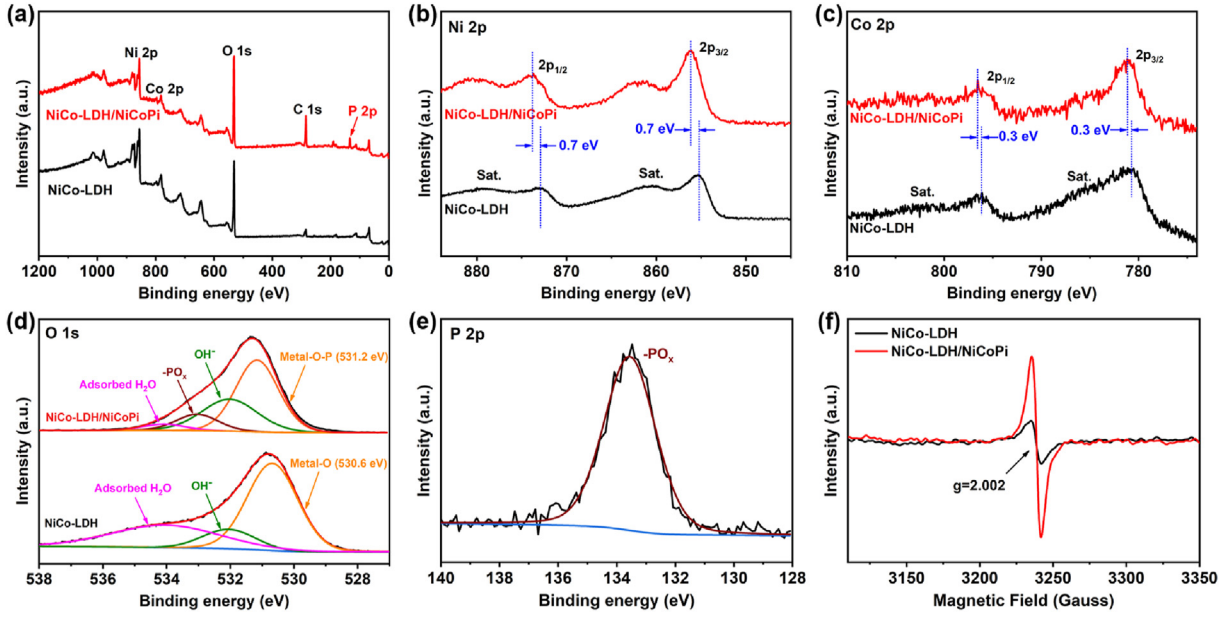

Fig. 3. (a) Survey XPS spectrum of NiCo-LDH and NiCo-LDH/NiCoPi; High-resolution XPS spectrum of (b) Ni 2p, (c) Co 2p, (d) O 1s and (e) P 2p of NiCo-LDH and NiCo-LDH/NiCoPi. (f) Electron paramagnetic resonance spectrum of NiCo-LDH and NiCo-LDH/NiCoPi.

oxygen vacancies [40], and the OH^-/Metal-O ratio in the NiCo-LDH/NiCoPi spectrum is about 0.59, which is about 2.5 times of that of pristine NiCo-LDH (0.23). This result can verify the additional oxygen vacancies in NiCo-LDH/NiCoPi resulting from the etching effect of PA during surface-neutralization. Finally, P atoms in the LDH/NiCoPi catalyst all exist in the form of phosphate groups as designed according to the P 2p spectrum (Fig. 3e) [42,43].

Further, Raman analysis was carried out to study the chemical vibration modes of NiCo-LDH/NiCoPi (Fig. S7). Two characteristic peaks at 463 and 517 cm^{-1} in the NiCo-LDH spectrum can be assigned to Metal-OH and Metal-O vibrations, respectively. The intensity of Raman peaks decreased after the PA surface-neutralization, accompanied by a redshift of the peak position, arising from the defects caused by the etching effect of PA and the interactions of phosphate groups with the metal sites [44,45]. The electron paramagnetic resonance (EPR) spectra were also collected to provide direct proof for oxygen vacancies (Fig. 3f). Compared to NiCo-LDH, the NiCo-LDH/NiCoPi catalyst exhibits a much stronger signal at g = 2.006, corresponding to the unsaturated oxygen vacancies, indicating a higher concentration of oxygen vacancies. Hence, the XPS, Raman, and EPR results all confirm that more oxygen defects were created during the PA surface-neutralization. The oxygen defects can improve the conductivity of the catalysts and expose more active sites for efficient OER [46,47].

Contact angle tests were conducted to study the effect of surface-neutralization on the surface property of NiCo-LDH. It can be seen that both NiCo-LDH and NiCo-LDH/NiCoPi show a hydrophilic feature in contrast with the bare NF, which shows a hydrophobic feature (Fig. S8a–c). A hydrophilic surface would benefit electrolyte diffusion and enable intimate contact between electrolyte and active sites [48]. Besides, easy gas bubble release from the catalyst is also essential for OER performance because the generated gas bubbles will obstruct active sites and hinder the OER process. As depicted in Fig. S8d–f, the NiCo-LDH/NiCoPi exhibited the largest bubble contact angle (150°) compared with that of NiCo-LDH (145°) and bare Ni foam (143°), indicating a more aerophobic surface, so that the produced O_2 bubbles can quickly release from the catalyst surface. Consequently, it is expected that the NiCo-LDH/NiCoPi exhibit a superior electrocatalytic activity towards OER.

3.2. OER electrocatalytic performance

Catalytic OER activity and stability of the as-synthesized catalysts were evaluated in a typical three-electrode cell in O_2-saturated 1 mol L^{-1} KOH electrolyte. The NiCo-LDH/NiCoPi catalyst performed superior electrocatalytic OER activity in 1 mol L^{-1} KOH electrolyte, as shown in Fig. 4a. Only a low overpotential of 300 mV was required to achieve 100 mA cm^{-2} OER, which is significantly lower than that of NiCo-LDH (373 mV) and IrO_2 (351 mV). A noticeable pre-oxidation peak of NiCo-LDH/NiCoPi between 1.3 and 1.5 V (vs. RHE) corresponds to the oxidation of metal species, which reveals the transformation of hydroxide to hydroxyl oxide during OER. The transformation of hydroxide to hydroxyl oxide during OER is an electrochemical deprotonation process [49], which could be promoted by phosphate groups due to its excellent proton transfer ability. Fig. S9 shows the enlarged LSV plots of NiCo-LDH and NiCo-LDH/NiCoPi. It

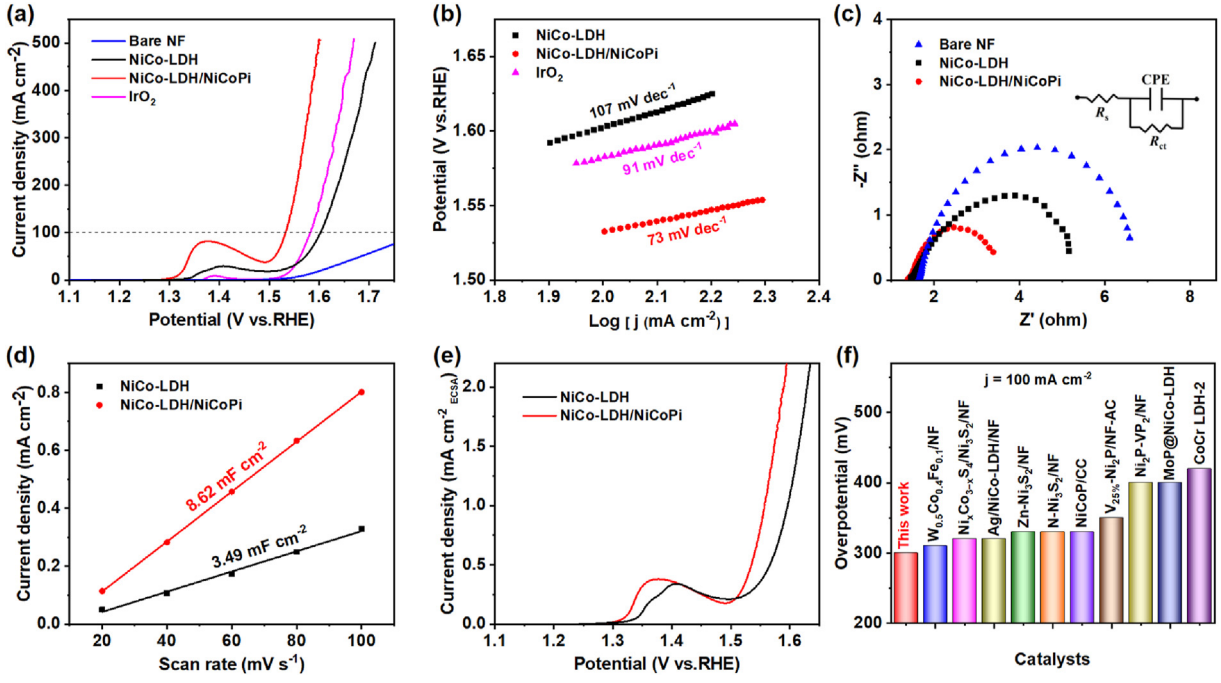

Fig. 4. (a) LSV plots of NiCo-LDH, NiCo-LDH/NiCoPi, IrO_2, and bare NF in 1 mol L^{-1} KOH electrolyte. (b) Corresponding Tafel slopes derived from the LSV plots. (c) Nyquist plots of Bare NF, NiCo-LDH and NiCo-LDH/NiCoPi. (d) Plots of charging current density versus the scan rates. (e) ECSA normalized OER activity of NiCo-LDH and NiCo-LDH/NiCoPi. (f) Comparison of the OER activity for NiCo-LDH/NiCoPi with reported catalysts, originating from Table S2.

can also be found that the onset potentials of the metal oxidation peaks were 1.28 and 1.30 V vs. RHE for the NiCo-LDH and NiCo-LDH/NiCoPi, respectively. Therefore, the phosphate heterojunction causes a 20-mV cathodic shift of the potential required to initiate the oxidation of the metal. The peak position also underwent a cathodic shift of 30 mV. The above result indicated the efficiency of phosphate heterojunction construction in promoting the formation of high-valence-state metal species at low overpotentials. And the oxidation peak for the NiCo-LDH/NiCoPi was notably larger than that of the NiCo-LDH, suggesting a higher population of the active hydroxyl oxide species in the NiCo-LDH/NiCoPi catalyst may contribute to its superior OER activity. Corresponding Tafel plots of the catalyst are illustrated in Fig. 4b. Compared to NiCo-LDH (107 mV dec^{-1}) and IrO_2 (91 mV dec^{-1}), the lowest Tafel slope of NiCo-LDH/NiCoPi (73 mV dec^{-1}) implies its fastest kinetics toward OER. Electrochemical impedance spectroscopy (EIS) spectra were collected to evaluate the charge transfer resistance (R_{ct}) of OER on different catalysts (Fig. 4c). The R_{ct} value of NiCo-LDH/NiCoPi is much smaller than NiCo-LDH, confirming the significantly improved charge transfer speed during the OER process on NiCo-LDH/NiCoPi mainly ascribed to the promotion effect of phosphate groups in NiCoPi. The intrinsic catalytic activity of NiCo-LDH/NiCoPi was also assessed by normalizing the LSV curves by the electrochemical active surface area (ECSA), which is calculated by the double-layer capacitance (C_{dl}) based on the cyclic voltammetry (CV) at various scan rates (Fig. 4d and Fig. S10). Higher activity was also observed for the NiCo-LDH/NiCoPi catalyst (Fig. 4e), indicating that heterointerface engineering can enhance the intrinsic activity of metal sites. The activity of NiCo-LDH/NiCoPi catalyst has also outperformed most reported non-precious catalysts, as depicted in Fig. 4f and Table S2. The higher intrinsic activity of the NiCo-LDH/NiCoPi catalyst might be originated from the excellent proton transfer ability of phosphate groups. In alkaline media, the OER process involves four consecutive proton-coupled electron transfer (PCET) steps on metal centers [50]:

$$M + OH^- \rightarrow MOH + e^- \quad (1)$$

$$MOH + OH^- \rightarrow MO + H_2O + e^- \quad (2)$$

$$MO + OH^- \rightarrow MOOH + e^- \quad (3)$$

$$MOOH + OH^- \rightarrow M + O_2 + H_2O + e^- \quad (4)$$

The deprotonation of surface intermediates plays a significant role in the OER process. As mentioned above, phosphate groups exhibit excellent proton transfer ability. Therefore, the NiCo-LDH/NiCoPi heterostructure can efficiently promote the deprotonation of surface intermediates (MOH and MOOH). The possible mechanisms are shown in Fig. S11. The phosphate groups in NiCoPi improve the proton-transfer kinetics, assisting the deprotonation steps from −OH to −O* and −OOH to −OO* during the OER.

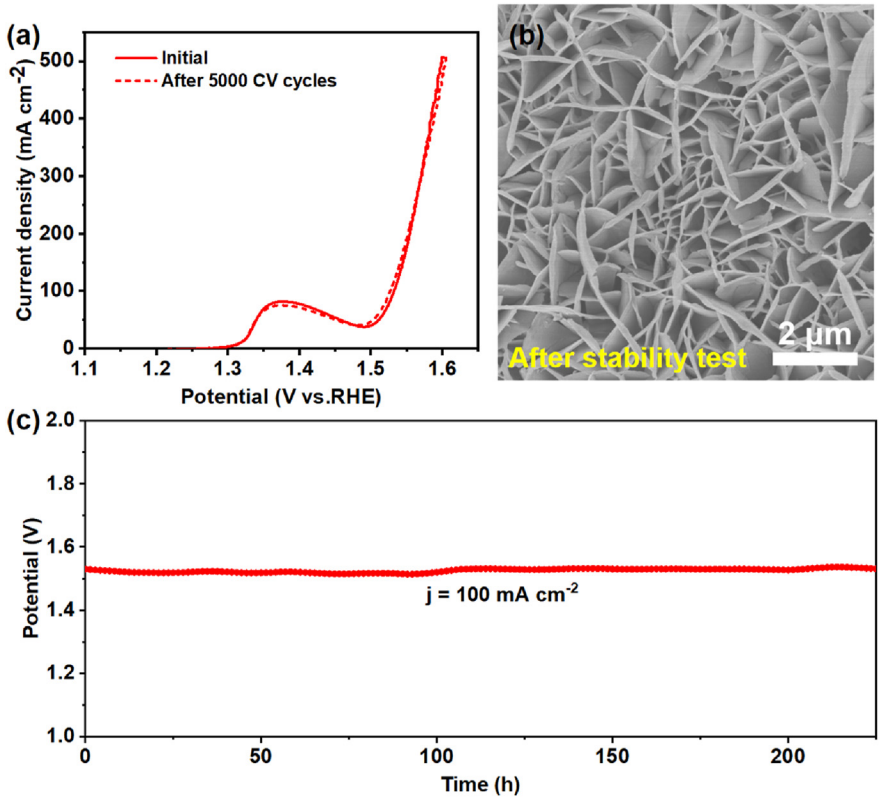

Fig. 5. (a) LSV plots of NiCo-LDH/NiCoPi before and after 5000 CV cycles in 1 mol L^{-1} KOH electrolyte. (b) SEM image of NiCo-LDH/NiCoPi after 5000 CV cycles. (c) CP curve of NiCo-LDH/NiCoPi at a constant current density of 100 mA cm^{-2} in 1 mol L^{-1} KOH electrolyte.

The stability of the NiCo-LDH/NiCoPi was subsequently evaluated by accelerated CV test and chronopotentiometry (CP) analysis. As shown in Fig. 5a, LSV plots obtained before and after 5000 CV cycles are nearly overlapped in 1 mol L^{-1} KOH electrolyte. The SEM (Fig. 5b) and TEM (Fig. S12) images evidences that the microstructure of NiCo-LDH/NiCoPi was well maintained after 5000 CV cycles, indicating its excellent structural stability. XPS is also performed to study the metal valence state change. As shown in Fig. S13, the ratio of Ni^{3+}/Ni^{2+} and Co^{3+}/Co^{2+} both dramatically increased, indicating that Ni and Co were oxidized to higher oxidation states corresponding to hydroxyl oxide species. The CP curve in Fig. 5c shows that the NiCo-LDH/NiCoPi can work continuously for more than 200 h at 100 mA cm^{-2} in 1 mol L^{-1} KOH electrolyte. The potential fluctuation after continuous testing at 100 mA cm^{-2} is only 5 mV, indicating the superior durability of NiCo-LDH/NiCoPi toward OER catalysis. The excellent catalytic activity and durability of NiCo-LDH/NiCoPi make it one of the best self-supported electrocatalysts for OER (Table S2).

Additionally, Raman tests were conducted to reveal the transformation of surface composition for NiCo-LDH/NiCoPi after the CP test (Fig. S14). The Raman spectrum shows a broad peak between 450 cm^{-1} and 700 cm^{-1}, proving hydroxyl oxide formation during OER. The surface-neutralization strategy is also suitable for improving the OER performance of other LDHs (Figs. S15–17), indicating the university of this method.

4. Conclusions

A facile surface-neutralization strategy was developed to construct TM-based LDH/NiCoPi hetero-sheets with abundant defects toward efficient and stable OER. The superior OER activity can be attributed to the modulated electronic structure of metal centers, the defect-rich structure and the promotion effect of Pi on proton transfer. In addition, the hydrophobic and aerophobic features promote electrolyte diffusion and easy gas bubble release. Thus, the as-synthesized catalyst (NiCo-LDH/NiCoPi) exhibits superior OER activity with a low overpotential of 300 mV to deliver 100 mA cm^{-2} OER and a Tafel slope of 73 mV dec^{-1}. Furthermore, the NiCo-LDH/NiCoPi catalyst can work continuously over 200 h at 100 mA cm^{-2} without visible activity decay. It can be concluded that this work provides a new and facile strategy for developing cost-effective and high-performance OER electrocatalysts.

Declaration of competing interest

The authors declare that they have no known competing financial interests or personal relationships that could have appeared to influence the work reported in this paper. The author Weiwei Cai is a Youth Editorial Board Member for Green Energy & Environment and was not involved in the editorial review or the decision to publish this article.

Acknowledgements

We are grateful for financial support from the National Natural Science Foundation of China (21875224 and 22179121), Knowledge Innovation Program of Wuhan-Basic Research (2022010801010202) and Research Fund Program of Guangdong Provincial Key Laboratory of Fuel Cell Technology (FC202201). The authors would like to thank SCI-GO (www.sci-go.com) for the contact angle analysis.

Appendix A. Supplementary data

Supplementary data to this article can be found online at https://doi.org/10.1016/j.gee.2022.12.003.

References

[1] Y.O. Wang, A. Vogel, M. Sachs, R.S. Sprick, L. Wilbraham, S.J.A. Moniz, R. Godin, M.A. Zwijnenburg, J.R. Durrant, A.I. Cooper, J.W. Tang, Nat. Energy 4 (2019) 746–760.
[2] J. Zhu, L.S. Hu, P.X. Zhao, L.Y.S. Lee, K.Y. Wong, Chem. Rev. 120 (2020) 851–918.
[3] Y.M. Shi, B. Zhang, Chem. Soc. Rev. 45 (2016) 1529–1541.
[4] Y. Wu, Y. Liu, K. Liu, L. Wang, L. Zhang, D. Wang, Z. Chai, W. Shi, Green Energy Environ. 7 (2022) 799–806.
[5] J.J. Song, C. Wei, Z.F. Huang, C.T. Liu, L. Zeng, X. Wang, Z.C.J. Xu, Chem. Soc. Rev. 49 (2020) 2196–2214.
[6] J. Kibsgaard, I. Chorkendorff, Nat. Energy 4 (2019) 430–433.
[7] Z. Liu, S. Xue, S. Zhou, J. Li, K. Qu, W. Cai, J. Catal. 405 (2022) 606–613.
[8] M. Yuan, Y. Sun, Y. Yang, J. Zhang, S. Dipazir, T. Zhao, S. Li, Y. Xie, H. Zhao, Z. Liu, G. Zhang, Green Energy Environ. 6 (2021) 866–874.
[9] D.J. Zhou, P.S. Li, X. Lin, A. Mckinley, Y. Kuang, W. Liu, W.F. Lin, X.M. Sun, X. Duan, Chem. Soc. Rev. 50 (2021) 8790–8817.
[10] X.-K. Gu, J.C.A. Camayang, S. Samira, E. Nikolla, J. Catal. 388 (2020) 130–140.
[11] D. González, J. Heras-Domingo, M. Sodupe, L. Rodríguez-Santiago, X. Solans-Monfort, J. Catal. 396 (2021) 192–201.
[12] M.-I. Jamesh, X. Sun, J. Power Sources 400 (2018) 31–68.
[13] P. Zhai, Y. Zhang, Y. Wu, J. Gao, B. Zhang, S. Cao, Y. Zhang, Z. Li, L. Sun, J. Hou, Nat. Commun. 11 (2020) 5462.
[14] D. González, M. Sodupe, L. Rodríguez-Santiago, X. Solans-Monfort, J. Catal. 412 (2022) 78–86.
[15] J. Li, J. Wu, Z. Xie, X. Zhang, S. Lv, H. Shao, K. Qu, W. Cai, Chem. Eng. J. 428 (2022) 131140.
[16] X. Zhang, Z. Song, Q. Yan, W. Cong, L. Yang, K. Zhu, K. Ye, J. Yan, D. Cao, G. Wang, J. Power Sources 515 (2021) 230627.
[17] S.L. Zhang, B.Y. Guan, X.F. Lu, S. Xi, Y. Du, X.W.D. Lou, Adv. Mater. 32 (2020) e2002235.
[18] Q. Wang, X. Huang, Z.L. Zhao, M. Wang, B. Xiang, J. Li, Z. Feng, H. Xu, M. Gu, J. Am. Chem. Soc. 142 (2020) 7425–7433.
[19] J. Li, J. Song, B.-Y. Huang, G. Liang, W. Liang, G. Huang, Y. Qi Jin, H. Zhang, F. Xie, J. Chen, N. Wang, Y. Jin, X.-B. Li, H. Meng, J. Catal. 389 (2020) 375–381.
[20] G. Liu, Y. Wu, R. Yao, F. Zhao, Q. Zhao, J. Li, Green Energy Environ. 6 (2021) 496–505.
[21] J.F. Yu, Q. Wang, D. O'hare, L.Y. Sun, Chem. Soc. Rev. 46 (2017) 5950–5974.

[22] M.P. Browne, Z. Sofer, M. Pumera, Energy Environ. Sci. 12 (2019) 41–58.
[23] H. Chi, J. Dong, T. Li, S. Bai, L. Tan, J. Wang, T. Shen, G. Liu, L. Liu, L. Sun, Y. Zhao, Y.-F. Song, Green Energy Environ. 7 (2022) 975–982.
[24] P. Zhai, M. Xia, Y. Wu, G. Zhang, J. Gao, B. Zhang, S. Cao, Y. Zhang, Z. Li, Z. Fan, C. Wang, X. Zhang, J.T. Miller, L. Sun, J. Hou, Nat. Commun. 12 (2021) 4587.
[25] J.-W. Zhang, X.-W. Lv, T.-Z. Ren, Z. Wang, T.J. Bandosz, Z.-Y. Yuan, Green Energy Environ. 7 (2022) 1024–1032.
[26] L. Dai, Z.N. Chen, L. Li, P. Yin, Z. Liu, H. Zhang, Adv. Mater. 32 (2020) e1906915.
[27] Q.Q. Liu, J.F. Huang, Y.J. Zhao, L.Y. Cao, K. Li, N. Zhang, D. Yang, L. Feng, L.L. Feng, Nanoscale 11 (2019) 8855–8863.
[28] J. Song, Y. Chen, H. Huang, J. Wang, S.C. Huang, Y.F. Liao, A.E. Fetohi, F. Hu, H.Y. Chen, L. Li, X. Han, K.M. El-Khatib, S. Peng, Adv. Sci. 9 (2022) e2104522.
[29] L.S. Xie, R. Zhang, L. Cui, D.N. Liu, S. Hao, Y.J. Ma, G. Du, A.M. Asiri, X.P. Sun, Angew. Chem. Int. Ed. 56 (2017) 1064–1068.
[30] D.J. Martin, G.G. Liu, S.J.A. Moniz, Y.P. Bi, A.M. Beale, J.H. Ye, J.W. Tang, Chem. Soc. Rev. 44 (2015) 7808–7828.
[31] H.Y. Qiao, X.Z. Wang, Q. Dong, H.K. Zheng, G. Chen, M. Hong, C.P. Yang, M.L. Wu, K. He, L.B. Hu, Nano Energy 86 (2021) 106029.
[32] N.L.W. Septiani, Y.V. Kaneti, K.B. Fathoni, J. Wang, Y. Ide, B. Yuliarto, Nugraha, H.K. Dipojono, A.K. Nanjundan, D. Golberg, Y. Bando, Y. Yamauchi, Nano Energy 67 (2020) 104270.
[33] C. Yang, C. Laberty-Robert, D. Batuk, G. Cibin, A.V. Chadwick, V. Pimenta, W. Yin, L. Zhang, J.M. Tarascon, A. Grimaud, J. Phys. Chem. Lett. 8 (2017) 3466–3472.
[34] J.Y. Xu, D.H. Xiong, I. Amorim, L.F. Liu, ACS Appl. Nano Mater. 1 (2018) 617–624.
[35] N.L.W. Septiani, Y.V. Kaneti, K.B. Fathoni, Y.N. Guo, Y. Ide, B. Yuliarto, X.C. Jiang, Nugraha, H.K. Dipojono, D. Golberg, Y. Yamauchi, J. Mater. Chem. A 8 (2020) 3035–3047.
[36] S.F. Li, Z.H. Liu, F.F. Wang, F.F. Yuan, Y.H. Ni, ACS Appl. Energy Mater. 4 (2021) 12836–12847.
[37] H. Sun, L. Chen, Y. Lian, W. Yang, L. Lin, Y. Chen, J. Xu, D. Wang, X. Yang, M.H. Rummerli, J. Guo, J. Zhong, Z. Deng, Y. Jiao, Y. Peng, S. Qiao, Adv. Mater. 32 (2020) e2006784.
[38] L. He, L. Gong, M. Gao, C.W. Yang, G.P. Sheng, Electrochim. Acta 337 (2020) 135799.
[39] K. Jin, J. Park, J. Lee, K.D. Yang, G.K. Pradhan, U. Sim, D. Jeong, H.L. Jang, S. Park, D. Kim, N.E. Sung, S.H. Kim, S. Han, K.T. Nam, J. Am. Chem. Soc. 136 (2014) 7435–7443.
[40] H. Ren, X. Sun, C. Du, J. Zhao, D. Liu, W. Fang, S. Kumar, R. Chua, S. Meng, P. Kidkhunthod, L. Song, S. Li, S. Madhavi, Q. Yan, ACS Nano 13 (2019) 12969–12979.
[41] Y.B. Li, C. Zhao, ACS Catal. 7 (2017) 2535–2541.
[42] N.L.W. Septiani, Y.V. Kaneti, K.B. Fathoni, K. Kani, A.E. Allah, B. Yuliarto, Nugraha, H.K. Dipojono, Z.A. Alothman, D. Golberg, Y. Yamauchi, Chem. Mater. 32 (2020) 7005–7018.
[43] D. Chinnadurai, M. Nallal, H.J. Kim, O.L. Li, K.H. Park, K. Prabakar, ChemCatChem 12 (2020) 2348–2355.
[44] R.L. Fan, Q.Q. Mu, Z.H. We, Y. Peng, M.R. Shen, J. Mater. Chem. A 8 (2020) 9871–9881.
[45] S.J. Liu, J. Zhu, M. Sun, Z.X. Ma, K. Hu, T. Nakajima, X.H. Liu, P. Schmuki, L. Wang, J. Mater. Chem. A 8 (2020) 2490–2497.
[46] M. Asnavandi, Y.C. Yin, Y.B. Li, C.H. Sun, C. Zhao, ACS Energy Lett. 3 (2018) 1515–1520.
[47] L.H. Zhuang, L. Ge, Y.S. Yang, M.R. Li, Y. Jia, X.D. Yao, Z.H. Zhu, Adv. Mater. 29 (2017) 1606793.
[48] Z.X. Wu, Y. Zhao, H.B. Wu, Y.X. Gao, Z. Chen, W. Jin, J.S. Wang, T.Y. Ma, L. Wang, Adv. Funct. Mater. 31 (2021) 2010437.
[49] W. Chen, B.B. Wu, Y.Y. Wang, W. Zhou, Y.Y. Li, T.Y. Liu, C. Xie, L.T. Xu, S.Q. Du, M.L. Song, D.D. Wang, Y.B. Liu, Y.F. Li, J.L. Liu, Y.Q. Zou, R. Chen, C. Chen, J.Y. Zheng, Y.F. Li, J. Chen, S.Y. Wang, Energy Environ. Sci. 14 (2021) 6428–6440.
[50] N.T. Suen, S.F. Hung, Q. Quan, N. Zhang, Y.J. Xu, H.M. Chen, Chem. Soc. Rev. 46 (2017) 337–365.